



# Performance-Enhancing Sulfur-Doped TiO<sub>2</sub> Photoanodes for Perovskite Solar Cells

Muhazri Abd Mutalib <sup>1</sup>, Norasikin Ahmad Ludin <sup>1,\*</sup>, Mohd Sukor Su'ait <sup>1</sup>, Matthew Davies <sup>2,3</sup>, Suhaila Sepeai <sup>1</sup> , Mohd Asri Mat Teridi <sup>1</sup>, Mohamad Firdaus Mohamad Noh <sup>1</sup> and Mohd Adib Ibrahim <sup>1</sup> 

- <sup>1</sup> Solar Energy Research Institute (SERI), Universiti Kebangsaan Malaysia (UKM), Bangi 43600, Selangor, Malaysia; muhazrimutalib@gmail.com (M.A.M.); mohdsukor@ukm.edu.my (M.S.S.); suhailas@ukm.edu.my (S.S.); asri@ukm.edu.my (M.A.M.T.); fir.noh@gmail.com (M.F.M.N.); mdadib@ukm.edu.my (M.A.I.)
- <sup>2</sup> SPECIFIC IKC, Materials Research Centre, College of Engineering, Swansea University Bay Campus, Fabian Way Institution, Swansea SA1 8EN, UK; m.l.davies@swansea.ac.uk
- <sup>3</sup> School of Chemistry and Physics, University of KwaZulu-Natal, Durban 4041, South Africa
- \* Correspondence: sheekeen@ukm.edu.my; Tel.: +60-(38)-9118586

**Abstract:** High-performance electron transport layer (ETL) anode generally needs to form a uniform dense layer with suitable conduction band position and good electron transport properties. The TiO<sub>2</sub> photoanode is primarily applied as the ETL because it is low-cost, has diverse thin-film preparation methods and has good chemical stability. However, pure TiO<sub>2</sub> is not an ideal ETL because it lacks several important criteria, such as low conductivity and conduction band mismatch with compositional-tailored perovskite. Thus, TiO<sub>2</sub> is an inefficient photo-anode or ETL for high-performance perovskite devices. In this study, sulfur as dopant in the TiO<sub>2</sub> photo-anode thin film is used to fabricate solid-state planar perovskite solar cells in relatively high humidity (40–50%). The deposited S-doped thin film improves the power conversion efficiency (PCE) of the device to 6.0%, with the un-doped TiO<sub>2</sub> producing a PCE of 5.1% in the best device. Improvement in PCE is due to lower recombination and higher photocurrent density, resulting in 18% increase in PCE (5.1–6.0%).

**Keywords:** perovskite solar cell; electron transporting material; TiO<sub>2</sub> photoanode; sulfur doping; photo conversion efficiency



**Citation:** Abd Mutalib, M.; Ahmad Ludin, N.; Su'ait, M.S.; Davies, M.; Sepeai, S.; Mat Teridi, M.A.; Mohamad Noh, M.F.; Ibrahim, M.A. Performance-Enhancing Sulfur-Doped TiO<sub>2</sub> Photoanodes for Perovskite Solar Cells. *Appl. Sci.* **2022**, *12*, 429. <https://doi.org/10.3390/app12010429>

Academic Editors:  
Laura Ciammaruchi and Beatriz Romero Herrero

Received: 30 October 2021  
Accepted: 2 December 2021  
Published: 3 January 2022

**Publisher's Note:** MDPI stays neutral with regard to jurisdictional claims in published maps and institutional affiliations.



**Copyright:** © 2022 by the authors. Licensee MDPI, Basel, Switzerland. This article is an open access article distributed under the terms and conditions of the Creative Commons Attribution (CC BY) license (<https://creativecommons.org/licenses/by/4.0/>).

## 1. Introduction

Perovskite solar cells (PSCs) have been attracting great attention in the past decade due to their rise in power conversion efficiencies (PCE), with certified efficiencies now greater than 25% [1–5]. A typical PSC consists of multiple layers of solid thin films, which include an electron transport layer (ETL), perovskite absorber layer and hole transport layer (HTL). These layers are aligned in the heterojunction according to its distinct device configurations. Regardless of the device configurations, an optimised ETL can potentially improve the overall behaviour of the PSCs in terms of the efficiency, hysteresis management and reproducibility of the device [6,7]. The functions of an ETL are closely related to its photoelectrochemical and structural properties by effectively facilitating electron collection and transfer from the photon-absorbing perovskite thin film. Good indications of a high-performance ETL or photo-anode include a thin, dense and suitable conduction band and good electron transfer. These characteristics also aim to minimise the interfacial recombination, facilitate electron movement and manage charge accumulation. The TiO<sub>2</sub> photo-anode is primarily applied as an ETL because it is low-cost, has numerous thin film preparation methods and has suitable chemical stability [8–10]. However, pure TiO<sub>2</sub> is not an ideal ETL because it lacks several important criteria such as low conductivity and conduction band mismatch with compositional-tailored perovskite (e.g., triple-cation perovskite system). Hence, there is room for improvement in the performance of TiO<sub>2</sub> as the ETL [1].

Metal doping of TiO<sub>2</sub> has become a practical technique to modify the band position and improve the thin film conductivity to fabricate photo-anodes with high charge extraction capacity. Dopants, such as yttria, niobium, magnesium and tin, have been proven to enhance the overall PSC efficiency due to the enriched layer conductivity and high electron mobility [11–14]. Although many dopants have been used to modify the TiO<sub>2</sub> photoanode for PSCs, the application of sulfur as dopant for these cells has not been reported yet. S-doped TiO<sub>2</sub> has been demonstrated to enhance photocurrent, light absorbance and photocatalytic activity and modify the band gap energy in other applications, such as coatings and photo-catalysis [15,16]. These properties could improve the characteristics of the photo-anode thin films for perovskite solar devices.

In this study, sulfur was used for the first time as dopant in the TiO<sub>2</sub> photo-anode thin film in solid-state planar heterojunction solar cells. Methylammonium lead iodide (CH<sub>3</sub>NH<sub>3</sub>PbI<sub>3</sub>) was used as the light absorber and spiro-OMeTAD as HTL. The effects of charge extraction and blocking of holes from the TiO<sub>2</sub> mesoporous layer was eliminated by choosing a planar PSC architecture. A sol-gel solution containing sulfur and titanium salts was spin coated onto the FTO glass to form the S-doped TiO<sub>2</sub> photo-anode thin film. The doping concentration of sulfur is tuned by controlling the sulfur salt content in the sol-gel solution.

## 2. Materials and Methods

Titanium diisopropoxide bis(acetylacetonate) (75 wt% in isopropanol), thiourea ( $\geq 99.0\%$ ), absolute ethanol (99.95%), acetylacetone ( $\geq 99\%$ ), lead iodide (PbI<sub>2</sub>, 99%), lithium bis(trifluoromethanesulfonyl)imide (Li-TFSI, 99%), 4-tert-butylpyridine (tBP, 96%), N,N-dimethylformamide (DMF, 99.8%), 2,20,7,70-tetrakis-(N,N-dip-methoxyphenylamine)-9,90-spirobifluorene (spiro-OMeTAD, SHT-263, Solarpur), tris(2-(1H-pyrazol-1-yl)-4-tert-butylpyridine) cobalt(III) tri[bis(trifluoromethane)sulfonimide] (FK209 Co(III) TFSI, 98%) and anhydrous acetonitrile (99.8%) were obtained from Sigma Aldrich and used as received. Prior to the deposition of photoanode layer, FTO-coated glass (FTO, TEC15, 15  $\Omega$ /sq, Great-cell Solar Materials) was first etched to design the desired pattern of electrode using zinc powder and 3M HCL. Next, the FTO substrate is cleaned using ultrasonic bath for 10 min, in the following order: soap (2% Hellmanex in water), acetone then propanol (99.5%), to remove the organic residue on the surface of FTO-glass substrate. In this modified sol-gel method, S-doped TiO<sub>2</sub> photoanode is prepared by first mixing 1.2 mL acetyl acetone, 7 mL TTIP, 35 mL absolute ethanol and calculated amounts of thiourea as sulfur source. To evaluate to effect of sulfur doping concentration, the amount of thiourea is prepared with 5%, 10% and 15% mol thiourea compared to TTIP. The precursor solution was then magnetically stirred for 180 min to produce a clear and homogeneous solution. A blank precursor solution was also prepared without the thiourea as control. The deposition of photoanode was carried out using spin coating method. 3 layers of TiO<sub>2</sub> photoanode was spin-coated at 3000 rpm with drying process at 120 °C for 10 min after each layer deposition. Afterwards, the TiO<sub>2</sub> photoanode was sintered at 450 °C to complete the deposition. The nomination of all sample relates to the sulfur doping content of the initial precursor solution.

To investigate the optical properties of the photoanode thin film, room temperature absorbance measurement (300 to 700 nm) is recorded using a UV-Vis spectrophotometer (Lambda 35, PerkinElmer). The XRD diffractogram of the photoanode thin film were analysed using X-ray diffractometer model Bruker D8 Advance (2 $\theta$ , 10–70°). The FTIR spectrum of TiO<sub>2</sub> photoanodes were evaluated using FTIR spectrometer (Shimadzu—840 s). Fluorescence spectroscopy was used to assess the charge recombination behaviours of TiO<sub>2</sub> photoanodes. The fluorescence spectroscopy analysis was carried out using a Perkin Elmer Luminescence spectrometer (LS 55) with a thin film holder accessory, at room temperature and 300 nm as excitation wavelength. Morphological study of the TiO<sub>2</sub> photoanodes were carried out using field-emission scanning electron microscopy (FESEM) were analysed using FE-SEM SUPRA VP55 equipped with an energy dispersive X-ray (EDX) spectroscopy for elemental detection and mapping. The photoelectrochemical (PEC) properties of

the TiO<sub>2</sub> photoanodes were determined via linear sweep voltammetry (LSV) using an electrochemical workstation (Metrohm Autolab), simulated AM 1.5 at a calibrated intensity 100 mWcm<sup>-2</sup> at NTP conditions. TiO<sub>2</sub> samples as the working electrode is immersed in Na<sub>2</sub>SO<sub>4</sub> solution (0.5 M), Pt as counter electrode and Ag/AgCl as the reference electrode. The scanning rate is kept at 20 mVs<sup>-1</sup> (-0.4 to 1.4 V vs. Ag/AgCl).

The perovskite solar devices were prepared by depositing the perovskite absorber layer, hole transporting layer and silver contact, consecutively. The perovskite absorber layer is deposited using a 2-step method where in the first layer, 100 µL of PbI<sub>2</sub> solution consisting of PbI<sub>2</sub> powder (507 mg) in DMF (1 mL) and tBP (100 µL) is spin coated on the TiO<sub>2</sub> photoanode at 3000 rpm for 30 s then annealed at 100 °C for 10 min. Previous study have emphasised the addition of tBP to enhance the hydrophobicity of PbI<sub>2</sub> and the deposited perovskite absorber [17]. Then, 250 µL of MAI solution consisting of 35 mg MAI powder in 1 mL isopropanol at 4000 rpm for 30 s then annealed at 100 °C for 30 min. After allowing the temperature to cool down to room temperature, hole transport layer solution is then spin coated at 4000 rpm for 30 s. The hole transport layer solution consisted of spiro-OMeTAD powder (72.3 mg), chlorobenzene (1 mL), 4-tert butylpyridine (28.8 µL), Li-TFSI solution (17.5 µL, 520 mg/mL in acetonitrile) and FK209 solution (29.0 µL, 520 mg/mL in acetonitrile). All of the perovskite solar devices layer solutions were prepared and spin coated in RH40-50%. To finish the perovskite solar devices, Ag counter electrode was thermal evaporated onto the hole transport layer under high vacuum atmosphere with 0.07 cm<sup>2</sup> active area. The photocurrent-voltage (I-V) characteristics were measured by applying a reverse scan at a rate of 0.1 V/s in a Keithley 2400 source meter under AM 1.5 G solar illumination. The average values of PSC devices were measured over 10 samples.

### 3. Results

#### 3.1. UV-Visible Spectroscopy

Given the boiling temperature of elemental sulfur at 444.6 °C, evaluating the behaviour of the S-doped TiO<sub>2</sub> thin film towards the change in sintering temperature is interesting. Figure 1a shows the UV-vis absorption spectra of various TiO<sub>2</sub> thin films sintered at 450 °C and 500 °C. The sintering temperatures were selected based on the temperature required to produce highly-crystalline TiO<sub>2</sub> thin films, that is, at least 450 °C [18]. 550 °C is not suitable due to the formation of rutile TiO<sub>2</sub> at this point, and this type of TiO<sub>2</sub> is less photo-active than anatase TiO<sub>2</sub> [19]. Firstly, all TiO<sub>2</sub> samples exhibit the typical absorbance behaviour of TiO<sub>2</sub> materials, in which the absorbance is low at higher wavelength and gradually increases at the UV region. Compared with the un-doped TiO<sub>2</sub> photo-anode, the S-doped TiO<sub>2</sub> displayed a small red shift of the absorption edge due to the new energy levels within the band gap caused by the doping of S. This phenomenon has been reported in a previous study [20,21]. Based on a previous study, the mechanism of TiO<sub>2</sub> band gap reduction could be attributed to the interaction between the S dopant (d and p orbitals) with the TiO<sub>2</sub> energy levels [22]. The bandgaps were reduced from 3.56 eV (un-doped TiO<sub>2</sub> photoanode) to 3.41 eV (10% S-doped TiO<sub>2</sub> photoanode) as estimated from the Tauc plots in Figure 1b. When the sintering temperature was increased to 500 °C, the absorption spectrum of the S-doped TiO<sub>2</sub> photoanode was reduced. This phenomenon suggested the S dopant has diffused out of the thin film, which was also found in a previous study [15]. Thus, to produce S-doped TiO<sub>2</sub> with anatase phase, 450 °C was selected as the sintering temperature.

The different doping levels of S were investigated using UV-vis spectroscopy. Figure 1b shows the absorption response of all S-doped TiO<sub>2</sub> photo-anodes with various concentrations of S. With 5% S dopant, the absorption bands were improved compared with those of the un-doped TiO<sub>2</sub> photo-anode. According to the plots, 10% S-doped TiO<sub>2</sub> showed the highest light absorbance. Thus, 10% was selected as the optimum concentration for sulfur doping.

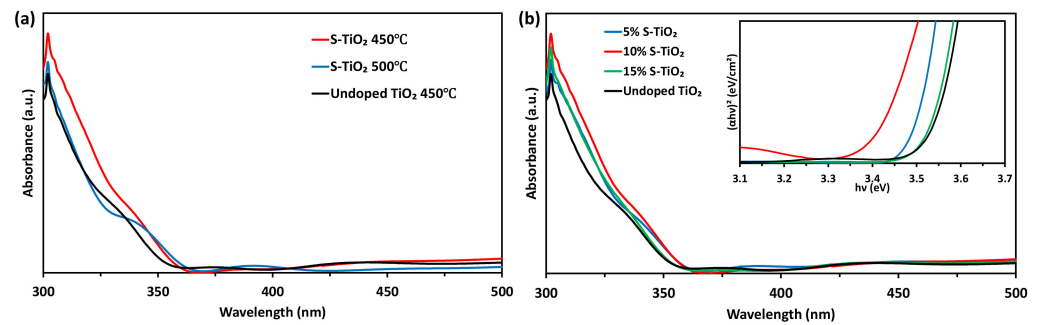


**Figure 1.** UV-Vis absorption spectra and Tauc plots (inset plot) of various TiO<sub>2</sub> photo-anodes (a) sintered at different temperatures and (b) with different loadings of S dopant.

### 3.2. X-ray Diffraction (XRD) Analysis

Changes in the crystalline phase of the S-TiO<sub>2</sub> photo-anode thin film were analysed using X-ray diffraction. The X-ray diffractograms of the un-doped and S-doped TiO<sub>2</sub> photo-anode thin film sintered at 450 °C are shown in Figure 2. Each sample had defined TiO<sub>2</sub> diffraction peaks, which were correlated with the characteristics of nano-crystalline anatase TiO<sub>2</sub> peaks with several FTO diffraction peaks. According to a previous study, the characteristic peaks of anatase TiO<sub>2</sub> are found at the angles of 27.0°, 38.2°, 55.1° and 62.0° corresponding to the (1 0 1), (1 0 4), (1 0 5) and (2 0 4) planes [23]. Rutile-phase TiO<sub>2</sub> was not found in the sintered TiO<sub>2</sub> photo-anode thin-film sample, which could be related to the sintering temperature of 450 °C. The sintering temperature is an important factor in producing the S-doped TiO<sub>2</sub> photo-anode thin film because a higher temperature could lead to the formation of un-desired, less photo-active rutile phase and could reduce the incorporation of S (boiling point: 444.6 °C) in the thin-film lattice [15]. The XRD diffractogram of the S-doped TiO<sub>2</sub> was compared with that of pure TiO<sub>2</sub>, and the two diffraction patterns were almost similar with no S characteristic peak. This observation indicated that the S ions had entered the lattice structure of TiO<sub>2</sub> or the concentration of the S compounds were lower than the detection limit of the equipment, as observed in a previous study [24]. In addition to the diffraction pattern, the data in the XRD pattern could be used to calculate the average particle size by using the Scherrer equation as follows:

$$D_{hkl} = \frac{0.89\lambda}{\beta \cos \theta} \quad (1)$$

where  $\lambda$  is the wavelength of the Cu K $\alpha$  laser used (0.1541 nm),  $\theta$  is the diffraction angle of the peak and  $\beta$  refers to the full width of the peak measured at half maximum intensity (FWHM) [25]. Thus, the average particle sizes of both samples were calculated according to Equation (1), resulting in 23.8 nm and 18.0 nm for the un-doped and S-doped TiO<sub>2</sub> photo-anode, respectively. Thus, S-doping had a direct effect on the average particle size of the sintered TiO<sub>2</sub> photo-anode. A previous study has reported that doping via substitution of a lattice atom with a dopant would reduce the grain size compared with the un-doped sample, as observed in this study [26].

### 3.3. Fourier-Transform Infrared (FTIR) Spectroscopy

The FTIR spectrum can be an effective tool to detect the functional groups in the TiO<sub>2</sub> thin films. Figure 3a shows the FTIR spectra of the S-doped and un-doped TiO<sub>2</sub> thin films. The broad absorption peak in the region between 1650 cm<sup>-1</sup> and 3450 cm<sup>-1</sup> could be associated to the O-H vibrations of the absorbed water molecules on the TiO<sub>2</sub> thin film surface (Figure 3a) [24,27]. Most importantly, the drop in the intensity in this region for the S-doped TiO<sub>2</sub> thin film would probably be attributed to the hydrophobicity of S. Close inspection of Figure 3b shows that the S distinct peak was absent in the un-doped TiO<sub>2</sub> sample but found in the S-doped TiO<sub>2</sub> sample. In a previous study, the distinct peak at 1086 cm<sup>-1</sup> and 1242cm<sup>-1</sup> corresponded to the characteristic of bidentate SO<sub>4</sub><sup>2-</sup>

co-ordination with metals, such as  $Ti^{4+}$ , and the formation of Ti-O-S bonds, respectively [22]. The presence of thiourea was negligible due to the absence of the C=O bond absorption bands. Thus, the FTIR spectra had proven the formation of S-doped  $TiO_2$  thin film by using the precursor solution and sintering at 450 °C to form the Ti-O-S bonds.

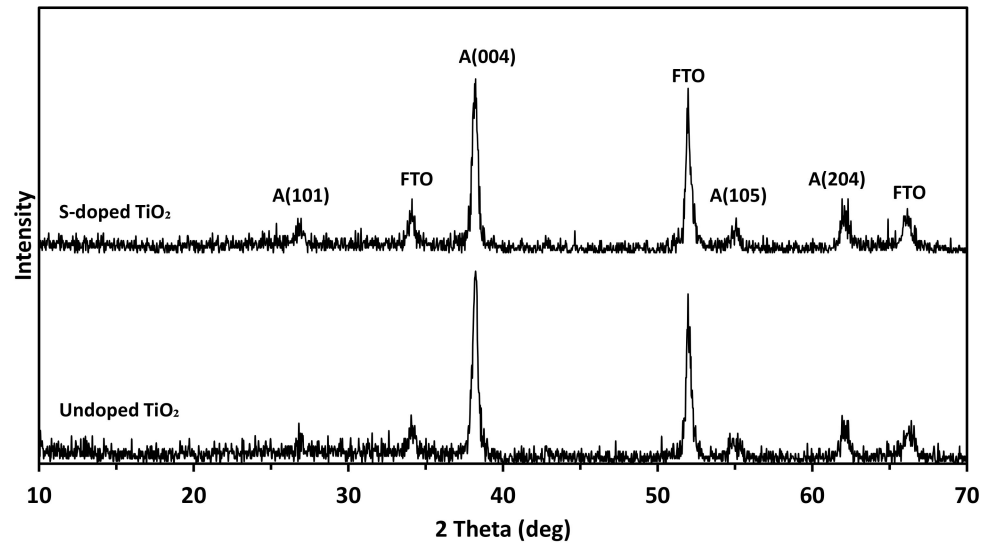


**Figure 2.** XRD diffractograms of the un-doped and S-doped  $TiO_2$  photo-anode thin films.

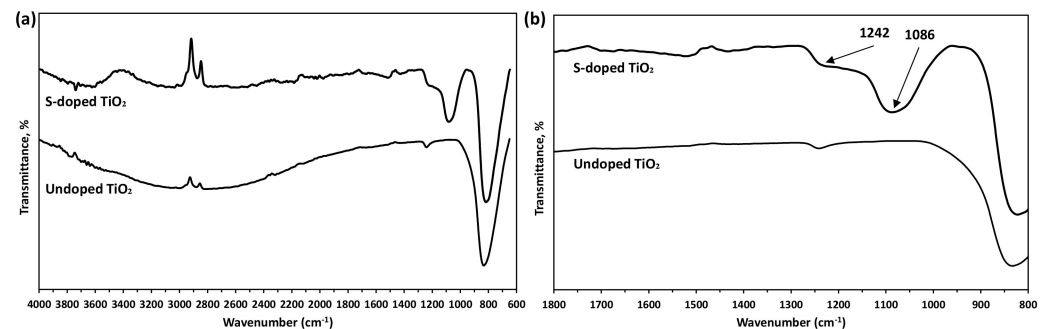


**Figure 3.** (a) FTIR spectrum and (b) sulfur characteristic absorption peaks of undoped and S-doped  $TiO_2$  ETL sintered at 450 °C.

### 3.4. Fluorescence Spectroscopy

Fluorescence emission spectroscopy is important to examine the ability of charge carrier trapping, migration and transfer and study the behaviour of electron/hole pairs in the semiconductor particles, such as  $TiO_2$  [28]. To elucidate the effects of S-doping on the recombination of the photo-generated electron/hole pairs produced in the  $TiO_2$  thin film, the fluorescence spectra were examined for the S-doped and un-doped  $TiO_2$ . Figure 4 illustrates the intensity of the fluorescence emission from the electron/hole recombination in the sample. The S-doped  $TiO_2$  thin film emits lower fluorescence intensity, which strongly suggested a lower radiative charge recombination and thus higher photo-catalytic efficiency [28]. Additionally, the produced fluorescence spectra showed similar patterns of peaks with only distinct intensities, which suggests that the addition of S in the  $TiO_2$  lattice did not change the  $TiO_2$  photo-catalytic mechanism.



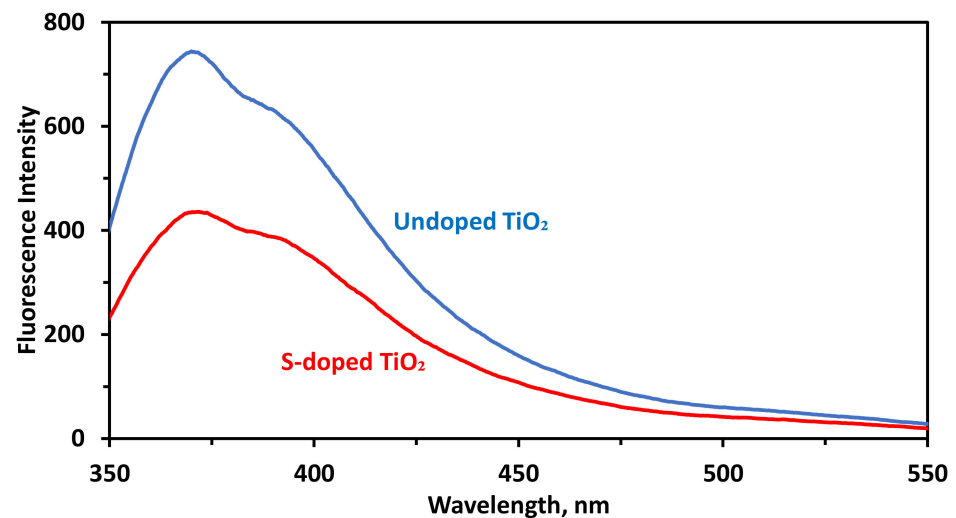


**Figure 4.** Fluorescence emission spectra of undoped and S-doped TiO<sub>2</sub> photoanode thin film.

### 3.5. Field Emission Scanning Electron Microscope (FESEM) Analysis

The effect of sulfur doping on the microstructure of the TiO<sub>2</sub> thin film photo-anode was assessed using the FESEM micrograph. Figure 5a,b indicate the FESEM morphological images of the un-doped and S-doped TiO<sub>2</sub> photo-anode thin films sintered at 450 °C, respectively. High-magnification images of the TiO<sub>2</sub> thin film revealed the nano-crystallisation of the deposited thin film, as suggested in the XRD diffractograms in Figure 2. Additionally, the thin film showed a dense and uniform morphology of homogenous granular and spherical grain. As mentioned in a previous study, the incorporation of S in the TiO<sub>2</sub> lattice would not contribute to a major change in the morphology of the thin film [22]. The EDX elemental spectra were recorded for the un-doped and S-doped TiO<sub>2</sub> thin films to observe the elements, as shown in Figure 5c,d, respectively. The EDX spectra for the S-doped TiO<sub>2</sub> thin film featured a minor peak for S at approximately 2.3 keV [24]. Additionally, the Ti peaks were observed at approximately 0.2 keV and a strong peak at 4.5 keV, which were attributed to the surface and bulk TiO<sub>2</sub>, respectively [29]. Figure 5e,f show the EDX elemental mapping of Ti, O and S in the un-doped and S-doped TiO<sub>2</sub> photo-anode thin films, respectively. The mapping images suggested the highly distributed behaviour of S ions throughout the S-doped TiO<sub>2</sub> thin film and the absence of S ions in the un-doped TiO<sub>2</sub> sample. Additionally, the presence of carbon in the S-doped TiO<sub>2</sub> photo-anode thin film most likely due to the usage of thiourea in the preparation of the thin film, as also described in previous study [30].

### 3.6. Linear Sweep Voltammetry (LSV) and Photocurrent–Voltage (J–V) Curve Studies

The photo-current response of the undoped and S-doped TiO<sub>2</sub> ETLs fabricated by spin-coating and sintered at 450 °C were evaluated using linear sweep voltammetry. The measurements were performed in the dark and under visible light-irradiated environment. The samples were soaked in 0.5 M Na<sub>2</sub>SO<sub>4</sub> solution at a scan rate of 20 mV/s, and the results are displayed in Figure 6a. At 1.0 V, the photo-current densities of the un-doped and S-doped samples were 0.0611 mA/cm<sup>2</sup> and 0.0695 mA/cm<sup>2</sup> (13.75% increase), respectively. Hence, the incorporation of S in the TiO<sub>2</sub> lattice increased the number of charge carriers (electron/hole pairs) in the photo-catalytic reaction of the thin film [23]. A previous study has reported similar responses, in which an increase in the photo-current to a certain extent was observed when the S content was increased, and a higher loading would be detrimental towards the photo-current readings due to the charge recombination of the electron-hole pair [31]. Thus, the incorporation of S as dopant could serve as a beneficial component to increase the photo-current in the thin film.

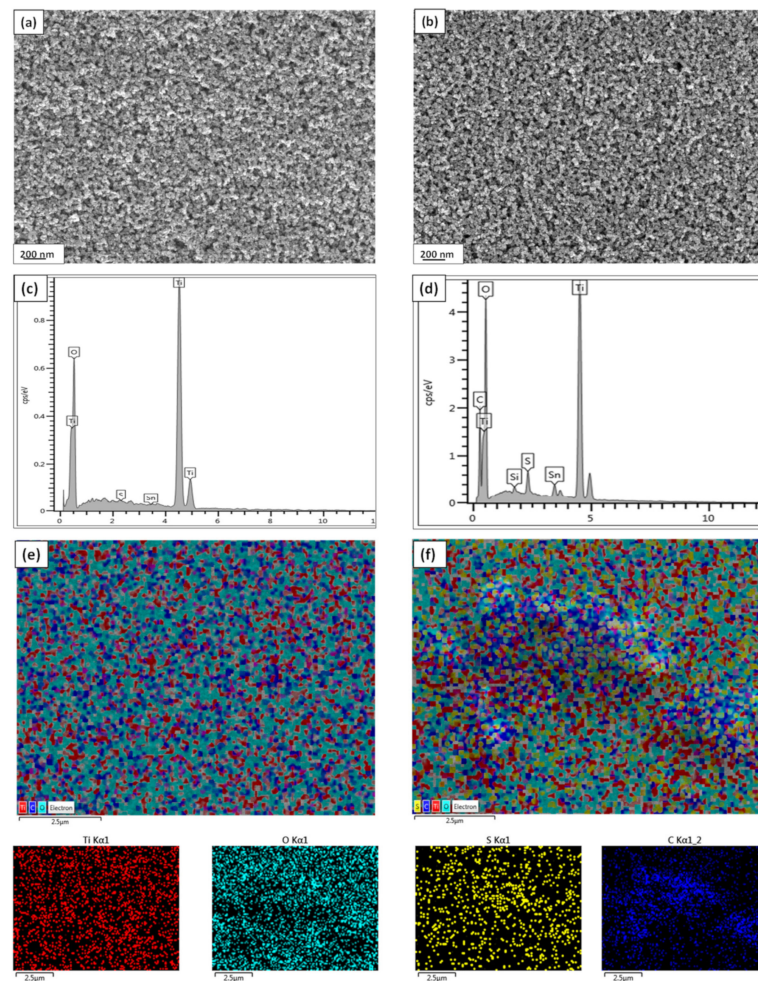


**Figure 5.** FESEM morphological images of the EDX elemental spectra and elemental mapping of Ti, O and S of the un-doped (a,c,e) and (b,d,f) S-doped  $\text{TiO}_2$ .

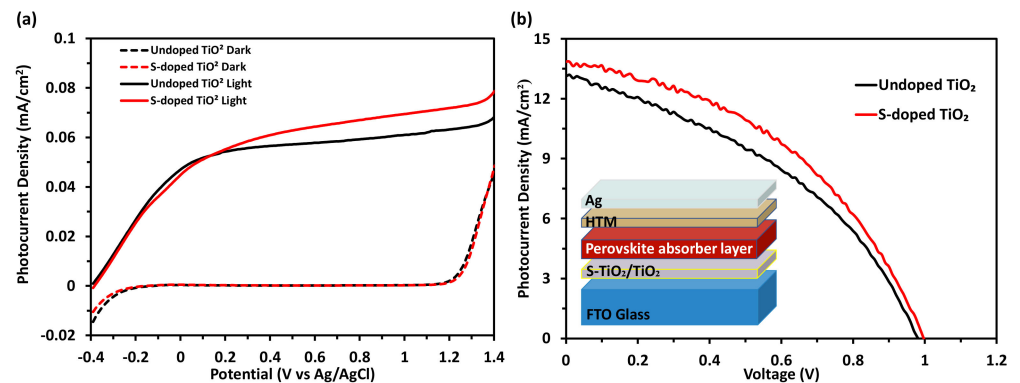


**Figure 6.** (a) LSV responses of the un-doped and S-doped  $\text{TiO}_2$  photo-anode in the dark and visible light-irradiated environment and (b) photo-current–voltage curve of the perovskite solar devices based on the S-doped  $\text{TiO}_2$  and  $\text{TiO}_2$  measured under standard AM1.5G illumination and the planar PSC structure (inset).

Perovskite solar devices with different photo-anodes were fabricated in high-humidity environment as described in the experimental procedure. Figure 6b (inset) shows the schematic diagram of the fabricated planar structured PSC in a relatively high humidity (40–50%). The photocurrent–voltage ( $J-V$ ) characteristic curves were observed under  $100 \text{ mW cm}^{-2}$  (1 sun) illumination. Figure 6b shows the  $J-V$  curve of the heterojunction perovskite solar devices based on the FTO/S-doped  $\text{TiO}_2$  or  $\text{TiO}_2/\text{CH}_3\text{NH}_3\text{PbI}_3/\text{spiro-}$

MeOTAD/Ag for the best device. The un-doped TiO<sub>2</sub> sample (reference device) produced a short-circuit density (J<sub>SC</sub>) of 13.1 mA cm<sup>-2</sup>, open circuit voltage of 0.982 mV, fill factor of 39.88% and PCE of 5.1%. By contrast, the S-doped perovskite device was improved with device performance of J<sub>SC</sub> of 13.9 mA cm<sup>-2</sup>, open circuit voltage of 0.997 mV, fill factor of 43.18% and PCE of 6.0%. The values of best device and device average over 10 made samples are summarised in Table 1. The device equipped with S-doped TiO<sub>2</sub> had better J<sub>SC</sub>, FF and PCE compared with the un-doped TiO<sub>2</sub>, but the V<sub>OC</sub> was relatively the same. The improvement in the J<sub>SC</sub> of the S-doped perovskite device was attributed to the increase in the electron collection capacity of the charge carrier and photo-current density, as described by Figure 6a, as reported in a previous study [1]. Additionally, Table 1 shows that the charge transfer resistance (R<sub>CT</sub>) in the S-doped TiO<sub>2</sub> perovskite device was lower than that of the un-doped TiO<sub>2</sub> device. The lower resistance could facilitate higher electron transfer in the perovskite device, resulting in the higher overall PCE.

**Table 1.** Photovoltaic parameters derived from J-V measurements for perovskite solar cells device using S-doped TiO<sub>2</sub> and undoped TiO<sub>2</sub> with a 0.07 cm<sup>2</sup> active area.

		J <sub>sc</sub> (mA/cm <sup>2</sup> )	V <sub>OC</sub> (V)	FF (%)	PCE (%)	R <sub>ct</sub> (Ω)
TiO <sub>2</sub>	Best	13.30	0.98	39.88	5.10	18.72
	Average	13.18 ± 0.08	0.97 ± 0.01	38.70 ± 0.77	4.98 ± 0.13	20.68 ± 1.54
S-doped TiO <sub>2</sub>	Best	13.9	0.997	43.18	6.0	14.26
	Average	13.65 ± 0.17	0.99 ± 0.003	42.19 ± 0.83	5.76 ± 0.19	14.68 ± 1.05

#### 4. Conclusions

In summary, the application of S-doped TiO<sub>2</sub> photo-anode as the ETL for planar PSC had been demonstrated. The optimized sintering temperature was 450 °C. The optimized sulfur dopant was 10% because a higher loading induced a drop in the absorbance capacity of the photo-anode. The S as dopant was proved to be present in the TiO<sub>2</sub> photo-anode layer after the deposition of S containing the precursor solution. The S-doped TiO<sub>2</sub> photo-anode was superior to the un-doped TiO<sub>2</sub> photo-anode in terms of higher absorbance, photocatalytic activity and photo-current density (13.75% increase). Perovskite solar devices with S-doped TiO<sub>2</sub> also showed better efficiency (18% increase) fabricated under relative humidity of 40–50%. The increase in the electron collection capacity of the carrier charge and photo-current density enhanced the PCE at 6.0%. Additional studies on the relation between hydrophobicity of ETL and stability of the PSC device should be performed. This work may facilitate the tailoring of the TiO<sub>2</sub> photo-anode to match the energy levels of an ETL with the perovskite absorber layer.

**Author Contributions:** Conceptualization, M.A.M. and N.A.L.; methodology, M.A.M.; software, M.A.M. and N.A.L.; validation, N.A.L., M.D. and M.A.I.; formal analysis, M.A.M.; investigation, M.A.M.; resources, M.F.M.N., M.A.M.T. and N.A.L.; data curation, M.A.M.; writing—original draft preparation, M.A.M. and N.A.L.; writing—review and editing, N.A.L., M.S.S., M.D. and S.S.; visualization, M.A.M., N.A.L. and M.D.; supervision, N.A.L.; project administration, N.A.L.; funding acquisition, N.A.L. All authors have read and agreed to the published version of the manuscript.

**Funding:** The authors acknowledge the financial support from the Universiti Kebangsaan Malaysia (UKM) under the Dana Impak Perdana (DIP-2019-025). The first author also wants to acknowledge the UKM for the PhD scholarship under the Skim Zamalah Yayasan Canselor.

**Institutional Review Board Statement:** Not applicable.

**Informed Consent Statement:** Not applicable.

**Acknowledgments:** The authors also appreciate the technical and management support from the Centre for Research and Instrumentation (CRIM), UKM.

**Conflicts of Interest:** The authors declare no conflict of interest.



## References

1. Su, T.S.; Wei, T.C. Co-Electrodeposition of Sn-Doped TiO<sub>2</sub> Electron-Transporting Layer for Perovskite Solar Cells. *Phys. Status Solidi Appl. Mater. Sci.* **2020**, *217*, 1900491. [[CrossRef](#)]
2. Abd Mutalib, M.; Ahmad Ludin, N.; Nik Ruzalman, N.A.A.; Barrioz, V.; Sepeai, S.; Mat Teridi, M.A.; Su'ait, M.S.; Ibrahim, M.A.; Sopian, K. Progress towards highly stable and lead-free perovskite solar cells. *Mater. Renew. Sustain. Energy* **2018**, *7*, 7. [[CrossRef](#)]
3. Mohamad Noh, M.F.; Arzaee, N.A.; Nawas Mumthas, I.N.; Mohamed, N.A.; Mohd Nasir, S.N.F.; Safaei, J.; Rashid bin Mohd Yusoff, A.; Nazeeruddin, M.K.; Mat Teridi, M.A. High-humidity processed perovskite solar cells. *J. Mater. Chem. A* **2020**, *8*, 10481–10518. [[CrossRef](#)]
4. He, R.; Ren, S.; Chen, C.; Yi, Z.; Luo, Y.; Lai, H.; Wang, W.; Zeng, G.; Hao, X.; Wang, Y.; et al. Wide-bandgap organic–inorganic hybrid and all-inorganic perovskite solar cells and their application in all-perovskite tandem solar cells. *Energy Environ. Sci.* **2021**, *14*, 5723–5759. [[CrossRef](#)]
5. Ahsan Saeed, M.; Hyeon Kim, S.; Baek, K.; Hyun, J.K.; Youn Lee, S.; Won Shim, J. PEDOT:PSS: CuNW-based transparent composite electrodes for high-performance and flexible organic photovoltaics under indoor lighting. *Appl. Surf. Sci.* **2021**, *567*, 150852. [[CrossRef](#)]
6. Mahmood, K.; Sarwar, S.; Mehran, M.T. Current status of electron transport layers in perovskite solar cells: Materials and properties. *RSC Adv.* **2017**, *7*, 17044–17062. [[CrossRef](#)]
7. Firdaus Mohamad Noh, M.; Hoong Teh, C.; Daik, R.; Liang Lim, E.; Chin Yap, C.; Adib, M.; Ahmad Ludin, N.; Rashid bin Mohd Yusoff, A.; Jang, J.; Asri Mat Teridi, M.; et al. The architecture of the electron transport layer for a perovskite solar cell. *J. Mater. Chem. C* **2017**, *6*, 682–712. [[CrossRef](#)]
8. Giordano, F.; Abate, A.; Correa Baena, J.P.; Saliba, M.; Matsui, T.; Im, S.H.; Zakeeruddin, S.M.; Nazeeruddin, M.K.; Hagfeldt, A.; Graetzel, M. Enhanced electronic properties in mesoporous TiO<sub>2</sub> via lithium doping for high-efficiency perovskite solar cells. *Nat. Commun.* **2016**, *7*, 10379. [[CrossRef](#)] [[PubMed](#)]
9. Abd Mutalib, M.; Aziz, F.; Fauzi, A.; Norharyati, W.; Salleh, W.; Yusof, N.; Jaafar, J.; Soga, T.; Zainizan, M.; Ahmad, N. Towards high performance perovskite solar cells: A review of morphological control and HTM development. *Appl. Mater. Today* **2018**, *13*, 69–82. [[CrossRef](#)]
10. You, Y.-J.; Saeed, M.A.; Shafian, S.; Kim, J.; Hyeon Kim, S.; Kim, S.H.; Kim, K.; Shim, J.W. Energy recycling under ambient illumination for internet-of-things using metal/oxide/metal-based colorful organic photovoltaics. *Nanotechnology* **2021**, *32*, 465401. [[CrossRef](#)]
11. Zhou, H.; Chen, Q.; Li, G.; Luo, S.; Song, T.B.; Duan, H.S.; Hong, Z.; You, J.; Liu, Y.; Yang, Y. Interface engineering of highly efficient perovskite solar cells. *Science* **2014**, *345*, 542–546. [[CrossRef](#)]
12. Lü, X.; Mou, X.; Wu, J.; Zhang, D.; Zhang, L.; Huang, F.; Xu, F.; Huang, S. Improved-performance dye-sensitized solar cells using Nb-doped TiO<sub>2</sub> electrodes: Efficient electron injection and transfer. *Adv. Funct. Mater.* **2010**, *20*, 509–515. [[CrossRef](#)]
13. Zhang, H.; Shi, J.; Xu, X.; Zhu, L.; Luo, Y.; Li, D.; Meng, Q. Mg-doped TiO<sub>2</sub> boosts the efficiency of planar perovskite solar cells to exceed 19%. *J. Mater. Chem. A* **2016**, *4*, 15383–15389. [[CrossRef](#)]
14. Cai, Q.; Zhang, Y.; Liang, C.; Li, P.; Gu, H.; Liu, X.; Wang, J.; Shentu, Z.; Fan, J.; Shao, G. Enhancing efficiency of planar structure perovskite solar cells using Sn-doped TiO<sub>2</sub> as electron transport layer at low temperature. *Electrochim. Acta* **2018**, *261*, 227–235. [[CrossRef](#)]
15. Arman, S.Y.; Omidvar, H.; Tabaian, S.H.; Sajjadnejad, M.; Fouladvand, S.; Afshar, S. Evaluation of nanostructured S-doped TiO<sub>2</sub> thin films and their photoelectrochemical application as photoanode for corrosion protection of 304 stainless steel. *Surf. Coat. Technol.* **2014**, *251*, 162–169. [[CrossRef](#)]
16. Niu, Y.; Xing, M.; Tian, B.; Zhang, J. Improving the visible light photocatalytic activity of nano-sized titanium dioxide via the synergistic effects between sulfur doping and sulfation. *Appl. Catal. B Environ.* **2012**, *115*, 253–260. [[CrossRef](#)]
17. Dong, G.; Ha, J.; Yang, Y.; Qiu, L.; Fan, R.; Zhang, W.; Bai, L.; Gao, W.; Fu, M. 4-Tert butylpyridine induced MAPbI<sub>3</sub> film quality enhancement for improving the photovoltaic performance of perovskite solar cells with two-step deposition route. *Appl. Surf. Sci.* **2019**, *484*, 637–645. [[CrossRef](#)]
18. Lee, H.; Hwang, D.; Jo, S.M.; Kim, D.; Seo, Y.; Kim, D.Y. Low-temperature fabrication of TiO<sub>2</sub> electrodes for flexible dye-sensitized solar cells using an electrospray process. *ACS Appl. Mater. Interfaces* **2012**, *4*, 3308–3315. [[CrossRef](#)] [[PubMed](#)]
19. Gao, S.A.; Xian, A.P.; Cao, L.H.; Xie, R.C.; Shang, J.K. Influence of calcining temperature on photoresponse of TiO<sub>2</sub> film under nitrogen and oxygen in room temperature. *Sens. Actuators B Chem.* **2008**, *134*, 718–726. [[CrossRef](#)]
20. Wu, M.C.; Chan, S.H.; Lee, K.M.; Chen, S.H.; Jao, M.H.; Chen, Y.F.; Su, W.F. Enhancing the efficiency of perovskite solar cells using mesoscopic zinc-doped TiO<sub>2</sub> as the electron extraction layer through band alignment. *J. Mater. Chem. A* **2018**, *6*, 16920–16931. [[CrossRef](#)]
21. Loan, T.T.; Huong, V.H.; Tham, V.T.; Long, N.N. Effect of zinc doping on the bandgap and photoluminescence of Zn<sup>2+</sup>-doped TiO<sub>2</sub> nanowires. *Phys. B Condens. Matter* **2018**, *532*, 210–215. [[CrossRef](#)]
22. Hamadani, M.; Reisi-Vanani, A.; Behpour, M.; Esmaeily, A.S. Synthesis and characterization of Fe,S-codoped TiO<sub>2</sub> nanoparticles: Application in degradation of organic water pollutants. *Desalination* **2011**, *281*, 319–324. [[CrossRef](#)]
23. Lei, J.; Li, X.; Li, W.; Sun, F.; Lu, D.; Yi, J. Arrayed porous iron-doped TiO<sub>2</sub> as photoelectrocatalyst with controllable pore size. *Int. J. Hydrogen Energy* **2011**, *36*, 8167–8172. [[CrossRef](#)]

24. Hamadani, M.; Reisi-Vanani, A.; Majedi, A. Preparation and characterization of S-doped TiO<sub>2</sub> nanoparticles, effect of calcination temperature and evaluation of photocatalytic activity. *Mater. Chem. Phys.* **2009**, *116*, 376–382. [[CrossRef](#)]
25. Wang, M.C.; Lin, H.J.; Yang, T.S. Characteristics and optical properties of iron ion (Fe<sup>3+</sup>)-doped titanium oxide thin films prepared by a sol-gel spin coating. *J. Alloys Compd.* **2009**, *473*, 394–400. [[CrossRef](#)]
26. Kment, S.; Kmentova, H.; Kluson, P.; Krysa, J.; Hubicka, Z.; Cirkva, V.; Gregora, I.; Solcova, O.; Jastrabik, L. Notes on the photo-induced characteristics of transition metal-doped and undoped titanium dioxide thin films. *J. Colloid Interface Sci.* **2010**, *348*, 198–205. [[CrossRef](#)] [[PubMed](#)]
27. León, A.; Reuquen, P.; Garín, C.; Segura, R.; Vargas, P.; Zapata, P.; Orihuela, P.A. FTIR and raman characterization of TiO<sub>2</sub> nanoparticles coated with polyethylene glycol as carrier for 2-methoxyestradiol. *Appl. Sci.* **2017**, *7*, 49. [[CrossRef](#)]
28. Basheer, C. Application of titanium dioxide-graphene composite material for photocatalytic degradation of alkylphenols. *J. Chem.* **2013**, *2013*, 456586. [[CrossRef](#)]
29. Nagaveni, K.; Hegde, M.S.; Madras, G. Structure and photocatalytic activity of Ti<sub>1-x</sub>M<sub>x</sub>O<sub>2±δ</sub> (M = W, V, Ce, Zr, Fe, and Cu) synthesized by solution combustion method. *J. Phys. Chem. B* **2004**, *108*, 20204–20212. [[CrossRef](#)]
30. Piątkowska, A.; Janus, M.; Szymański, K.; Mozia, S. C-, N- and S-Doped TiO<sub>2</sub> Photocatalysts: A Review. *Catalysts* **2021**, *11*, 144. [[CrossRef](#)]
31. Kumari, S.; Chaudhary, Y.S.; Agnihotry, S.A.; Tripathi, C.; Verma, A.; Chauhan, D.; Shrivastav, R.; Dass, S.; Satsangi, V.R. A photoelectrochemical study of nanostructured Cd-doped titanium oxide. *Int. J. Hydrogen Energy* **2007**, *32*, 1299–1302. [[CrossRef](#)]